ACS APPLIED NANO MATERIALS

www.acsanm.org Article

Surface Functionalization of $CsPbBr_3$ Nanocrystals for Photonic Applications

Andreas Manoli, Paris Papagiorgis, Marios Sergides, Caterina Bernasconi, Modestos Athanasiou, Sergey Pozov, Stelios A. Choulis, Maryna I. Bodnarchuk, Maksym V. Kovalenko, Andreas Othonos, and Grigorios Itskos*

Cite This: *ACS Appl. Nano Mater.* 2021, 4, 5084−5097

Read Online

ACCESS | Metrics & More | Article Recommendations | Supporting Information

ABSTRACT: The primary obstacle to the use of lead halide perovskite nanocrystals (NCs) in optoelectronics is the inability of traditional ligand engineering approaches to provide robust surface passivation. The structural lability can be mitigated by employing different ligands such as long-chain quaternary ammonium and zwitterionic surfactants. Here, we report a comprehensive study that probes the impact of such surface passivation routes on the optoelectronic properties of weakly confined $CsPbBr_3$ NCs. Spectroscopy unravels clear correlations of various photophysical figures of merit with the ligand type used. Compared to NCs decorated by conventional oleic acid/oleylamine ligands, passivation with the quaternary ammonium or zwitterionic surfactants increases the NC solid-state emission yield by up to 40% by halving the average trap depth and increasing by 1.5 times the exciton binding energy. Furthermore, the aforementioned ligands better preserve the size of NCs in thin films, as shown by the absence of significant NC aggregation and the confinement-induced increase by a factor of 2 of the Fröhlich interaction between excitons and optical phonons. The suitability of ligands for photonics is finally assessed by probing metrics, such as the amplified spontaneous emission threshold, the moisture tolerance, and the photoconductivity and electroluminescent performance of lateral and vertical devices, respectively.

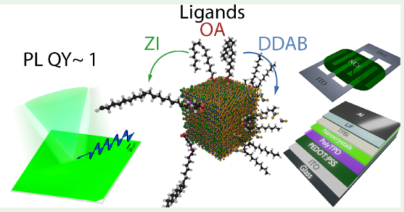

KEYWORDS: *perovskites, lead halides, nanocrystals, optical properties, spectroscopy, surface passivation*

INTRODUCTION

Lead halide perovskite nanocrystals (LHP NCs) have rapidly emerged as viable contenders for the next generation of classical and quantum light-emitting devices owing to their outstanding characteristics, in terms of tunability, efficiency, chromaticity, and optical coherence.[1−5] Their unique emission characteristics largely stem from their defect-tolerant electronic structure, which, in theory, allows such NCs to emit brightly, even without overcoating with epitaxial wide-gap shells, but as long as surface Pb ions are well passivated. In reality, surface chemistry plays a key role in tackling a major deficiency of such NCs related to the softness of the material and the dynamic nature of ligand binding, which renders LHP NCs colloidally and structurally unstable. Various synthesis methods, summarized into three main strategies, have been employed to circumvent such lability: (i) the addition of new ligand complexes;[6−13] (ii) the application of postsynthetic, passivation treatment;[14−20] and (iii) the incorporation into various host matrices.[21−29] Among the most successful and practical approaches, a combination of the ligand and postsynthetic passivation strategies was implemented to produce robust $CsPbBr_3$ NCs with near-unity emission quantum yields (QYs), for instance, using didodecyldimethylammonium bromide (DDAB) complexes[9,10,30] and long-chain zwitterionic (ZI) ligands.[6] The simplicity and the highly successful outcome of the two treatments make them a highly promising surface-functionalization protocol for producing stable and bright $CsPbBr_3$ NCs for applications and devices.

Photoluminescence (PL) serves as a universally suited probe for monitoring the surface state of NCs. The impact of surface treatment and the extent to which surface traps are healed are typically quantified by the enhancement of the PL QY and the modification, i.e., typical lengthening, of the PL lifetime. Herein, we use a comprehensive spectroscopic and device approach with a view of exploring, in more detail, the influence of the two aforementioned ligand treatments on the optoelectronic properties of weakly confined $CsPbBr_3$ NCs. In particular the impact of surface passivation by the conventional oleic acid/oleylamine (OA) ligands, the ZI 3-(*N*,*N*-dimethyloctadecylammonio)propansulfonate molecule, and two kinds of DDAB-based treatments is comprehensively and quantitatively evaluated by obtaining and analyzing an extended list of photophysical and device figures of merit at the low (exciton

Received: February 24, 2021
Accepted: May 7, 2021
Published: May 19, 2021

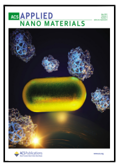

occupancy per NC ~0.1) and high (occupancy up to 10 excitons per NC) excitation regime.

■ EXPERIMENTAL SECTION

Material Synthesis. (i) $CsPbBr_3$ NCs capped with OA were synthesized following the procedure described in ref 2; a 1:1 ratio (v/v) of oleic acid and oleylamine was used; (ii) DDAB was synthesized following the procedure described in ref 10; (iii) DDAB−lead bromide (DDAB/$PbBr_2$) were synthesized following the procedure described in ref 10; and (iv) the ZI ligand sulfobetaine were synthesized following the procedure described in ref 6.

Transmission Electron Microscopy. Transmission electron microscopy (TEM) images were collected using a JEOL JEM-2200FS microscope operated at 200 kV.

Film Processing. All studied films were fabricated under ambient conditions, out of material solutions with a concentration of ~25 g/L in toluene via spin coating at 1000 rpm for 1 min on 1 cm^2 quartz substrates using an Ossila Spin Coater followed by a drying step at 500 rpm for 30 s. The substrates were cleaned with nitric acid (HNO_3) and de-ionized water. To achieve thick films, the dried substrates were treated with triethoxy(octyl)silane in toluene (1:100 v/v).

Optical Spectroscopy. Optical absorption was recorded using a PerkinElmer Lambda 1050 spectrophotometer equipped with a three-detector module covering the 300−3000 nm spectral range. Continuous wave PL was carried out on a 0.35 m FluoroLog FL3 Horiba Jobin Yvon spectrofluorometer equipped with a TBX-04 PMT. The samples were excited using an unfocused 405 nm laser diode at a low fluence (5 mW/cm^2) of $\langle N \rangle$ ~0.2. The calculation of the average exciton occupancy per NC was performed based on the method reported in ref 31. The acquired spectra were corrected for the spectral response of the grating and detector and were normalized to the absorbance of each film at the excitation wavelength to take into account thickness variations between films. PL excitation (PLE) experiments were carried out on the same setup, using the monochromator-filtered output of a 450 W ozone-free Xe lamp. The spectra obtained were normalized to the intensity of the excitation source.

Time-resolved PL (TR-PL) was measured on the same spectrometer using a time-correlated single-photon counting system. The samples were excited by a 405 nm NanoLED laser diode with a pulse width of ~50 ps, operating at 100 kHz to avoid NC photocharging. To allow spatial averaging over the probed samples, multiple spots per sample were probed. The PL decays were obtained while monitoring the PL emission peak with a spectral bandwidth of ~8 nm.

Temperature-dependent steady-state PL (SS-PL) experiments in the range of 10−340 K were performed with samples placed on a Janis closed-cycle optical refrigerator. Variable temperature TR-PL measurements were performed in the 80−340 K range using a Janis liquid nitrogen optical cryostat.

Ultrafast time-resolved pump-probe absorption measurements were carried out using a mode-locked Ti:sapphire ultrafast amplifier generating ~100 fs pulses at 800 nm running at a repetition rate of 250 kHz. A nonlinear β-barium borate crystal was used to frequency double the amplifier output at 400 nm with an energy of 1.3 mJ per pulse. The beam served as the pump excitation pulse. A fraction of the fundamental beam was used to generate a super continuum light for probing at different QD energy states in the 420−750 nm range. Measurements were carried out using a typical pump-probe optical setup in a noncollinear configuration, where differential transmission was measured as a function of optical delay between the pump and the probe pulses. The probing wavelengths were spectrally analyzed via a fast linear array coupled to a spectrometer combined with a synchronized optical chopper at the amplifier repetition rate.

Device Fabrication and Characterization. *Light-Emitting Diodes (PeLEDs).* Bottom emission light-emitting diodes were fabricated using the following device structure: ITO/PEDOT:PSS-(AI4083)/PolyTPD/NC/TPBi/LiF/Al. ITO substrates were subsequently cleaned with acetone and isopropanol under sonication for 10 min and then dried and exposed to UV-ozone treatment for 10 min. The ~40 nm poly(3,4-ethylenedioxythiophene) polystyrene sulfonate (PEDOT:PSS) AI4083 (Heraeus) films were coated using static spin coating (Delta 6RC-Suss MicroTec, Garching, Germany) at 4000 rpm for 30 s, followed by annealing at 140 °C for 20 min, under an ambient atmosphere. Subsequently, ~40 nm poly(*N*,*N*′-bis-4-butylphenyl-*N*,*N*′-bisphenyl)benzidine (PolyTPD) films (M_w = 55k Da, Ossila Ltd.), 6 mg/mL in chlorobenzene, were spin coated at 2000 rpm for 30 s, followed by annealing at 150 °C for 15 min, under ambient conditions. $CsPbBr_3$ NC thin films in the range of 10−20 nm were spin coated at 6000 rpm for 60 s under an ambient atmosphere, and then, the samples were transferred into a nitrogen atmosphere glovebox for the thermal evaporation of the top electrode. To complete the device stack, 40 nm (1 A/s) 2,2′,2″-(1,3,5-benzinetriyl)-tris(1-phenyl-1-*H*-benzimidazole) (TPBi) (Ossila Ltd.), 1 nm (0.2 A/s) lithium fluoride (LiF) (Kurt J. Lesker), and 100 nm (2 A/s) of aluminum (Al) (Kurt J. Lesker) were thermally evaporated in a vacuum chamber (Angstrom Engineering, Kitchener, Canada) at a base pressure of $\sim 2 \times 10^{-6}$ mbar through a shadow mask, resulting in an active device area of 9 mm^2. As a final step, all the devices were encapsulated using a glass slide and a UV-curable encapsulation epoxy from Ossila Ltd. The PeLEDs were characterized using current density−voltage−luminance characteristics (JVL), using a Botest LIV Functionality Test System with a calibrated silicon photodiode sensor (spectral sensitivity of 350−730 nm and responsivity of 60 nA/lx). All the measurements were performed under ambient conditions.

Lateral Photoconductive Devices. The solution (70 μL) was spin coated at 1000 rpm for 60 s, followed by a drying step at 4000 rpm for 30 s on an interdigited ITO substrate with a contact distance of 50 μm (Ossila). The photocurrent of the devices was measured with a Keithley 2461 under 405 nm and 90 mW/cm^2 excitation with the help of an epi-fluorescence microscope so that only the area around the contacts was excited.

■ RESULTS AND DISCUSSION

Materials and Basic Properties. $CsPbBr_3$ NCs capped with OA, DDAB, DDAB/$PbBr_2$, and ZI ligands exhibit a cuboid shape with average particle sizes of ~8.8 ± 0.6, 9.2 ± 0.6, 9.3 ± 0.8, and 9.1 ± 0.6 nm, respectively, as shown in the TEM images of Figure 1a−d and TEM analysis in Figure S1. The optical properties of the respective diluted NC solutions are displayed in Figure S2, while representative absorption, PL emission, and PLE spectra from spin-cast films of the NCs are displayed in Figure 1e−h. The absorption edge coincides with the PLE peak in all NC types, providing a reliable estimation of the band edge in the solid state. A weak, higher energy feature at ~2.95 eV, observed in the PLE of OA-, DDAB-, and DDAB/$PbBr_2$-capped NCs, as well as in the absorption of the DDAB/$PbBr_2$-capped NC spectra, is probably associated with a van Hove singularity of $CsPbBr_3$ at the M point of the Brillouin zone.[32,33] For the OA-capped NC film, absorption and PLE indicate an energy gap of ~2.435 eV, shifted by ~30 meV to a lower energy compared to the respective value in the colloidal phase (see Figure S2). In contrast, the band edge of the NC solutions and films for the DDAB-, DDAB/$PbBr_2$-, and ZI-capped NCs are in closer energetic proximity, i.e., ~9, ~1, and ~5 meV, respectively.

Figure 1i−l shows the representative fluorescence microscope images of the NCs under study. DDAB-based NC films exhibit the most uniform surface topography, with a slightly rougher surface for the NCs, in which a combined treatment with DDAB and $PbBr_2$ was used. Importantly, the fluorescence images taken contain no evidence of significant NC aggregation effects, confirming the strong DDAB surface binding that effectively preserves the particle size and shape upon ligand exchange.[34,35] For the ZI-capped NC films, the relatively uniform distribution of the NC emission is perturbed by a small number of micron-scale, bright-emitting NC clusters, as representatively depicted

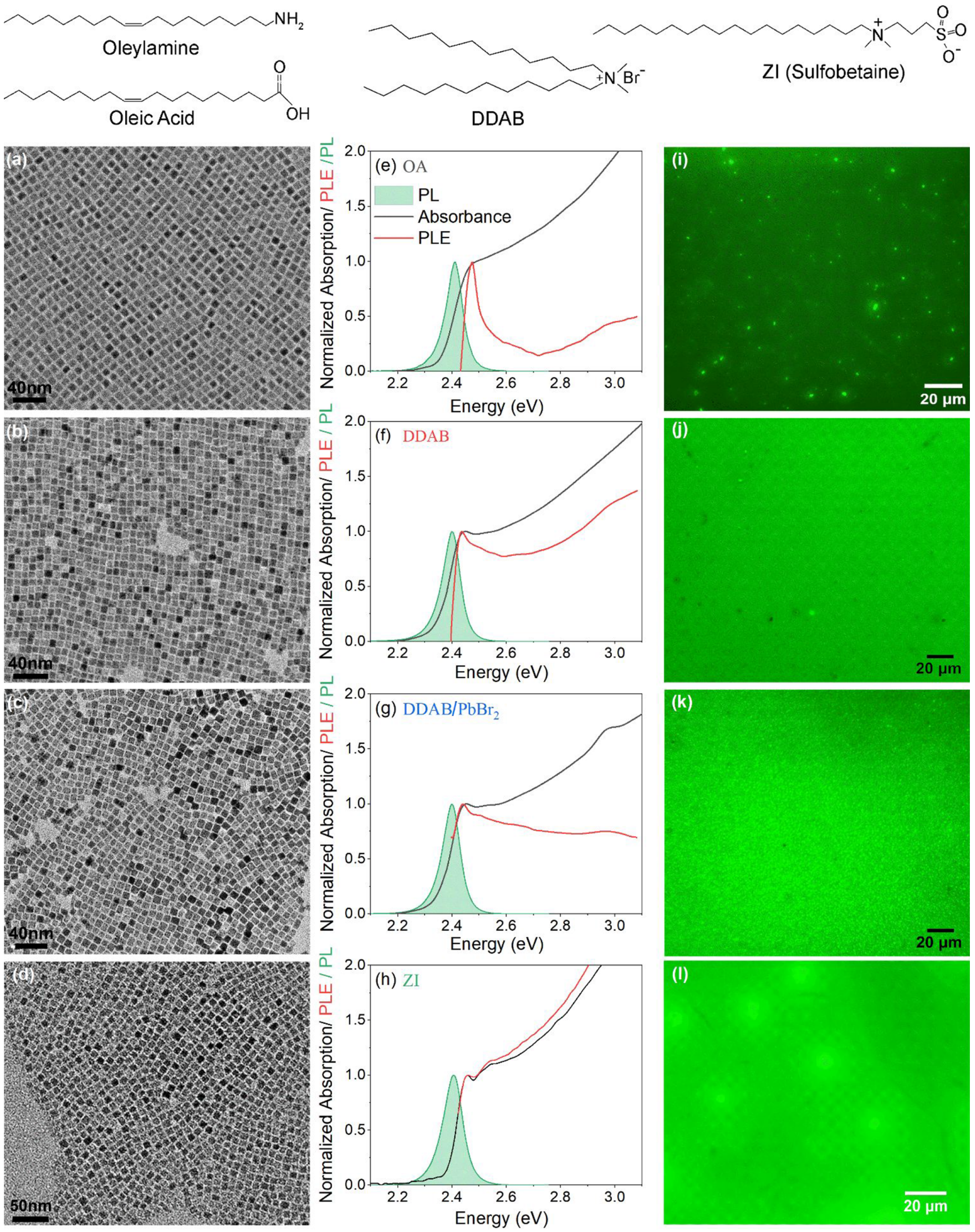

Figure 1. TEM images of (a) OA-, (b) DDAB-, (c) DDAB/PbBr$_2$-, and (d) ZI-capped CsPbBr$_3$ NCs. Optical absorption, PL, and PLE spectra of (e) OA-, (f) DDAB-, (g) DDAB/PbBr$_2$-, and (h) ZI-capped NC films. Representative fluorescence microscope images of the respective films are displayed in (i)−(l). At the top of the figure, the chemical structures of the four ligands used in the study are displayed.

in Figure 1l. The formation of such larger crystals appears characteristic of the NC−NC interactions mediated by the ZI ligands as they are present in all films studied. OA-capped NC films on the other hand, contain a higher density of light-emitting NC agglomerations attributed to NC necking because of ligand desorption.

The observation is consistent with the substantial larger red shift of the emission of such NC films, compared to their PL in the colloidal state, mentioned above. Despite the extensive NC sintering, the PL QY of the OA-capped NCs is quite high, with an average value of ~68 ± 8% estimated using integrating sphere measurements as well as statistics from different studied films. The measured QY lies within the 60−80% range reported in several publications for the solid-state QY of OA-capped CsPbBr$_3$ NCs.[6,15,36] The high QY indicates that the merging of the NCs because of ligand detachment is not detrimental to the emission properties of such solids; yet even brighter emitters can be obtained, exploiting the improved surface passivation by

https://doi.org/10.1021/acsanm.1c00558
ACS Appl. Nano Mater. 2021, 4, 5084−5097

Table 1. Parameters Extracted from the Curve Fitting of the Emission Line Width for the Studied NC Systems[a]

capping	Γ_0 (meV)	γ_{AC} (μeV/K)	γ_{LO} (meV)	E_{LO} (meV)	γ_{imp} (meV)	E_{LO}^{exp} (meV)
OA	38	82 ± 5	51 ± 4	34 ± 3	~0	35
DDAB	26	74 ± 6	69 ± 3	30 ± 1	~0	31
DDAB/$PbBr_2$	28	40 ± 5	95 ± 4	30 ± 4	~0	36
zwitterion	30	39 ± 2	111 ± 8	33 ± 3	~0	37

[a] The last column shows the energy of the dominant LO phonon mode observed at low-temperature Raman spectroscopy spectra.

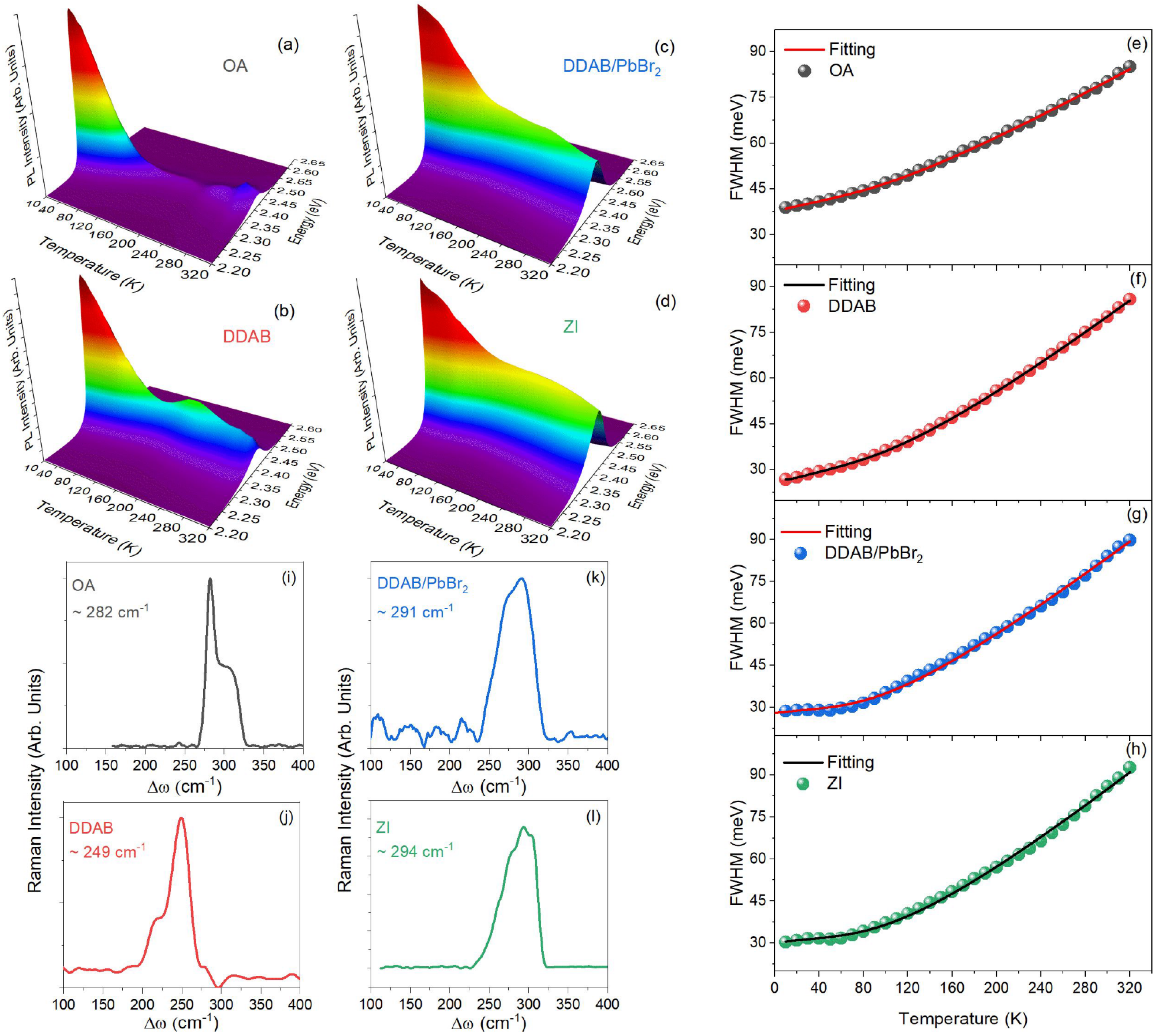

Figure 2. Variable-temperature PL contour plots of (a) OA-, (b) DDAB-, (c) DDAB/$PbBr_2$-, and (d) ZI-capped $CsPbBr_3$ NC films. PL FWHM vs temperature from the (e) OA-, (f) DDAB-, (g) DDAB/$PbBr_2$-, and (h) ZI-capped NCs. The black line indicates the fitting described by eq 1. Raman scattering spectra obtained at 10 K from (i) OA-, (j) DDAB-, (k) DDAB/$PbBr_2$-, and (l) ZI-capped NCs.

the other studied ligands, as evidenced by the increase in the QY to 85 ± 6%, 89 ± 4%, and 95 ± 4% for the DDAB-, DDAB/$PbBr_2$-, and ZI-capped NCs, respectively. PL QY values above 80% have been reported for DDAB- and DDAB/$PbBr_2$-capped $CsPbBr_3$ NCs,[15,37−39] while values approaching unity have been demonstrated in ZI-capped NCs.[6,36,40]

Photophysics at Low Photoexcitation Densities. Exciton recombination in low photoexcitation conditions of exciton occupancy $\langle N \rangle \sim 0.2$ was probed via variable temperature PL experiments in the 10−340 K range; the raw data in the form of three-dimensional contour plots are presented in Figure 2a−d for the studied NC films.

The variation of the PL line shape with temperature, displayed in Figure 2e−h, is initially discussed. The temperature evolution of the FWHM in the four samples is modeled using eq 1,[34] which evaluates the contribution of homogeneous and inhomogeneous emission broadening mechanisms in the NCs:

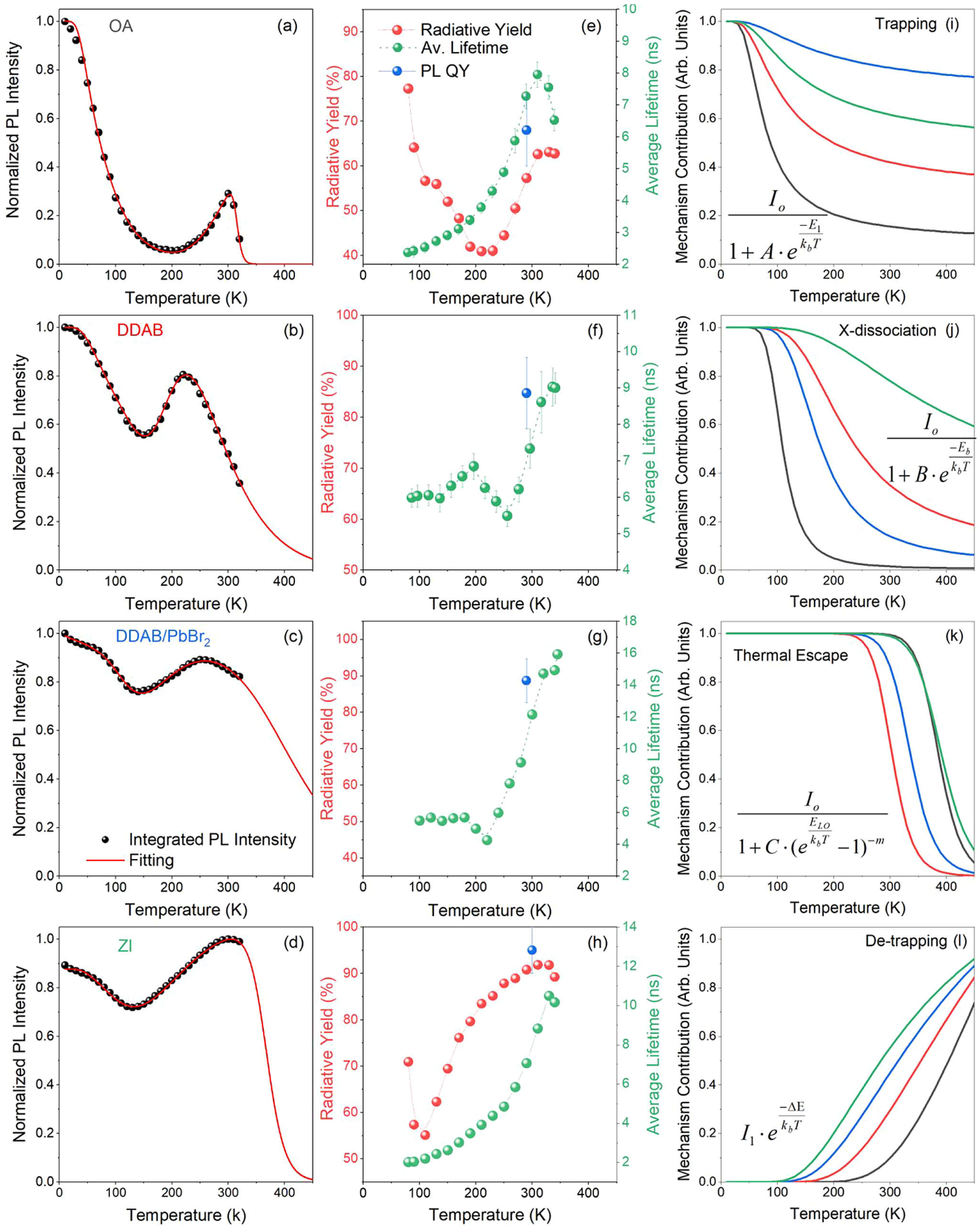

Figure 3. Integrated PL intensity vs temperature for the (a) OA-, (b) DDAB-, (c) DDAB/PbBr$_2$-, and (d) ZI-capped CsPbBr$_3$ NCs. The red line indicates the fitting by the Arrhenius model of eq 2. Radiative yield and average PL lifetime of (e) OA-, (f) DDAB-, (g) DDAB/PbBr$_2$-, and (h) ZI-capped CsPbBr$_3$ NCs. In all cases, the blue symbols display the PL QY average value and respective uncertainty obtained by integrating sphere measurements and statistics. (i−k) Arrhenius functions of each exciton recombination channel, when the other channels are deactivated. The quenching functions are normalized to T = 0 K. (l) Enhancement functions normalized to T = 500 K.

$$\Gamma(T) = \Gamma_0 + \gamma_{AC}T + \frac{\gamma_{LO}}{e^{-E_{LO}/k_BT} - 1} + \gamma_{imp}e^{-E_b/k_BT} \quad (1)$$

In the equation, Γ_0 characterizes the temperature-independent inhomogeneous broadening because of NC size distribution and lattice imperfections. γ_{AC} and γ_{LO} are the acoustic and optical exciton−phonon coupling constants that define the broadening because of the exciton−acoustic phonon interaction and the exciton−LO phonon interaction, respectively. The last term describing scattering in ionized impurities is considered, which is quantified by the coupling term γ_{imp}. The fitting extracted parameters are presented in Table 1. It can be observed that the temperature-independent broadening term Γ_0 assumes the highest value on the OA-capped NCs. The larger Γ_0 value cannot be attributed to a larger NC size distribution, as all studied samples exhibit more or less the same size distribution width, as indicated by the analysis shown in Figure S1. Instead, the larger inhomogeneous broadening reflects the higher spatial and energetic disorder of such NCs in the solid state, as evidenced by the PL data and microscopy results presented earlier. It can be also seen that, in agreement with numerous optical and transport studies on LHPs, the contribution of the impurity scattering term γ_{imp} is negligible.[41−43]

As expected for polar inorganic semiconductors, temperature-dependent emission broadening is dominated by strong interactions with LO phonons[44] with high coupling strength

https://doi.org/10.1021/acsanm.1c00558
ACS Appl. Nano Mater. 2021, 4, 5084−5097

Table 2. Parameters Extracted from the Modified Arrhenius Model Fit

capping	ΔE (meV)	q^a	E_1 (meV)	$E_{LO}{}^a$ (meV)	E_b (meV)	m	$E_{th}{}^b$ (meV)
OA	49 ± 1	2	16 ± 1	34	62 ± 2	10 ± 2	340 ± 74
DDAB	32 ± 2	2	15 ± 2	30	80 ± 5	10 ± 3	300 ± 90
DDAB/$PbBr_2$	26 ± 1	2	22 ± 3	30	85 ± 1	9 ± 2	270 ± 60
zwitterion	24 ± 3	2	14 ± 3	33	100 ± 4	10 ± 2	330 ± 66

[a] The parameters q and E_{LO} were fixed. [b] E_{th} was calculated by the product of E_{LO} and m.

in the range of 50−110 meV, similar to that previously measured in $CsPbBr_3$ NCs.[41,45−47] As exciton−optical phonon interaction prevails, coupling to the acoustic phonons appears suppressed, yet non-negligible, as the omission of the relevant linear term in eq 1 reduces significantly the fit accuracy at low temperatures. The fit indicates that the excitons interact with longitudinal optical phonons with energies E_{LO} in the 30−34 meV range, similar to the reported values in ref47 but overall overestimated compared to the literature consensus on nanocrystal and bulk crystals of $CsPbBr_3$,[41,44−49] in which carrier-interacting LO phonon modes of 16−23 meV are reported. Fits, in which the parameter E_{LO} was deliberately fixed within the aforementioned range, exhibit notably larger regression standard errors and thus reduced goodness compared to the reported model. To provide further insight into the apparent inconsistency, we performed low-temperature (10 K) Raman scattering experiments on the same NC films in which the temperature-dependent PL measurements were carried out. Raman measurements yield a reliable probe of the exciton−phonon interaction, with excitons actively participating in the inelastic process as intermediate states.[50] The Raman spectra, shown in Figure 1i−l, dominated in all cases, by a broad manifold of high-energy optical modes, peaked at energies of 250−300 cm^{-1} (31−37 meV). Such energies well match the fit-extracted LO-phonon energies, validating our model accuracy. Furthermore, the results appear consistent with a recent terahertz spectroscopy-based study, reporting on blue-shifted optical phonon modes in ZI-capped $CsPbBr_3$ NCs,[51] compared to bulk $CsPbBr_3$ crystals. Inspection of Table 1 also reveals an interesting ligand-dependent variation of the exciton−acoustic γ_{AC} and the exciton−optical γ_{LO} phonon coupling terms, with the latter increasing at the expense of the former as more robust surface passivation methodologies such as DDAB/$PbBr_2$ and the ZI ligands are implemented. In polar semiconductors, γ_{LO} predominantly accounts for the Fröhlich interaction of charged carriers, i.e., electrons and holes composing the excitons with the electric field of the LO phonons, which, in the case of $CsPbBr_3$, are predominantly associated with the optical vibrations of the $PbBr_6$ octahedra.[49] In the DDAB- and ZI-capped NCs, the $PbBr_2$ sublattice is fairly intact, as such ligands well preserve and even restore the damaged $PbBr_6$ octahedra.[6,10] The field of the LO phonons in the intact $PbBr_6$ octahedra[49] of such NCs is robust and results in stronger interactions with excitons, compared to OA-capped NCs, in which ligand desorption alters the surface stoichiometry and damages the $PbBr_2$ cage, resulting in the weakening of the optical phonon−exciton interaction. Thus, the strength of the Fröhlich interaction between excitons and optical phonons, quantified by the γ_{LO} coupling, appears to be directly correlated with the structural robustness of the material, providing an additional metric of the surface quality of $CsPbBr_3$ NCs.

The integrated PL intensity as a function of temperature for the four types of NC films is presented in Figure 3a−d.

In all samples, the temperature increase results in the expected quenching of the emission as nonradiative exciton recombination is thermally activated. The emission drop is accompanied by an intermediate temperature regime in which a nontypical PL enhancement occurs before emission suppression at temperatures higher than 300 K occurs. The anomalous increase in the PL intensity with temperature has been observed in both all-inorganic[45] and hybrid[52] perovskite NCs, being assigned to thermally activated exciton detrapping processes, effectively increasing the NC exciton population that participates in the radiative recombination process. What is important here is that the characteristics of such emission enhancement, i.e., the relative emission gain and the temperature range in which the PL rise is activated and peaked, depend on the ligand type used to passivate the NCs.

To quantify the contribution of each exciton quenching and enhancement mechanism, the data were fitted using the following modified Arrhenius equation:[53]

$$I(T) = \frac{I_0 + I_1\, e^{-(\Delta E/k_B T)^q}}{1 + A\, e^{-E_1/k_B T} + B\, e^{-E_b/k_B T} + C(e^{E_{LO}/k_B T} - 1)^{-m}} \tag{2}$$

In the model, I_0 is the PL intensity at zero temperature; I_1 is the emission because of excitons that are thermally detrapped from traps of depth ΔE and distribution defined by q; E_b is the binding energy of the exciton; and E_{LO} is the longitudinal optical phonon energy, with m being the number of LO phonons required to transfer sufficient kinetic energy to excitons for thermal escape, i.e., average thermal escape barrier $E_{th} = m \times E_{LO}$. Fit at low temperatures requires the inclusion of a third activation term characterized by the energy E_1. A, B, and C are the parameter factors of the aforementioned processes. To reduce the number of the fit adjustable parameters, the trap state distribution was assumed to be Gaussian, assigning the value of 2 to parameter q. Furthermore, the LO phonon energies were fixed to the respective values produced by the PL line width model, considering that such values have been independently confirmed by the Raman scattering experiments. The model produces good fits of the data for all four types of NCs samples, as observed in Figure 3a−d, with the fit-extracted parameters presented in Table 2.

The ligand-dependent contribution of each recombination process can be quantified by the values of the parameters E_1, E_{LO}, m, and E_b that define the activation energy of the process and the respective factors A, B, and C that account for each channel strength. However, the latter factors are entangled in eq 2; hence, a direct comparison of their magnitude in the different NCs studied is not meaningful. Instead, we can obtain useful insights by plotting the Arrhenius functions displayed in Figure 3i−k, which include the contribution of each activated quenching term as if it was the only recombination process in which the NCs were imposed to. For comparative purposes, the functions are normalized to T = 0 K.

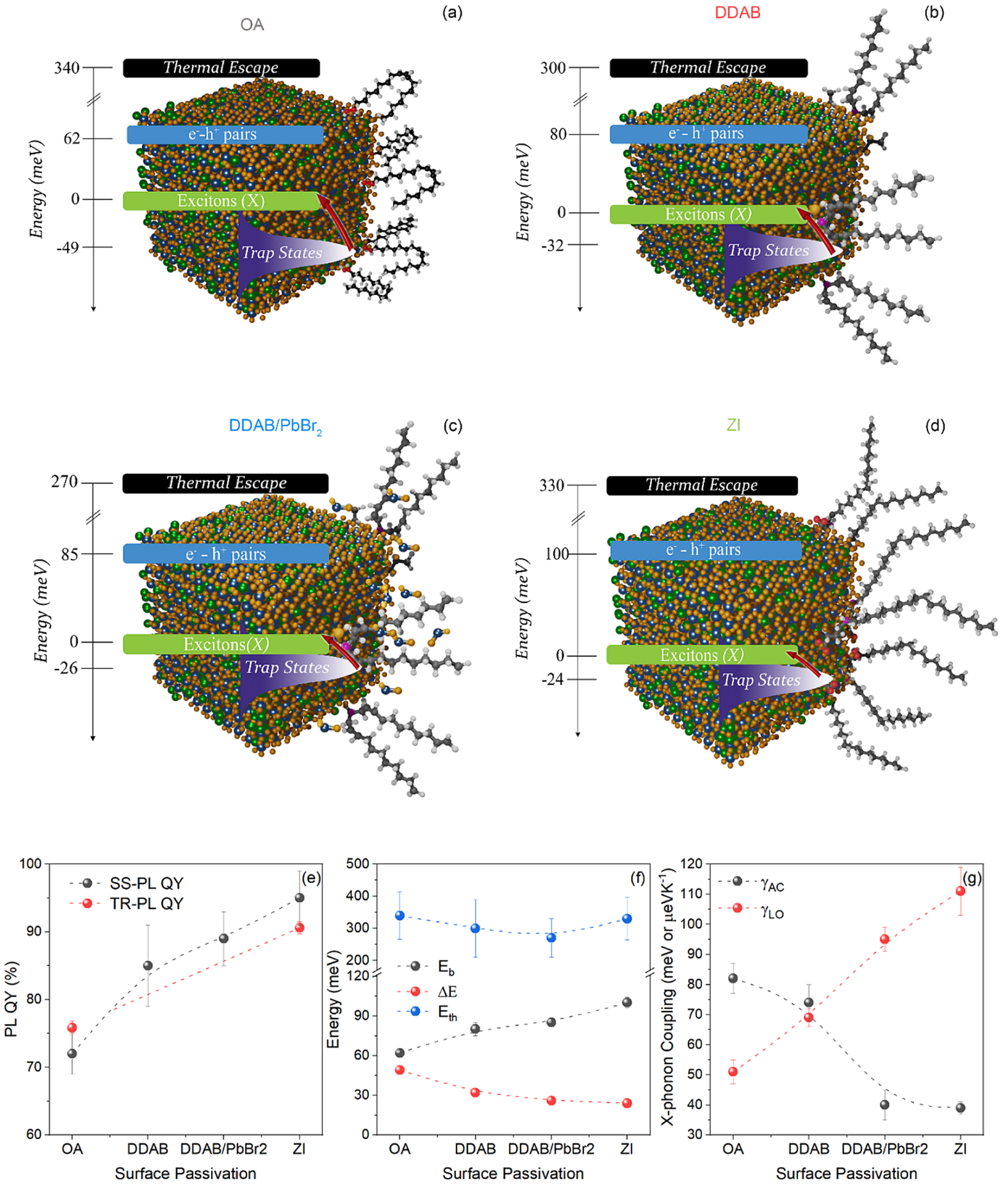

Figure 4. Illustration of (a) OA-, (b) DDAB-, (c) DDAB/PbBr$_2$-, and (d) ZI-capped NCs. Each schematic contains the estimated average energy levels of uncorrelated electron–hole pairs, excitons, and defects along with the confinement potential of each NCs. (e) PL QY from integrating sphere, SS-PL experiments (SS-PL QY), and TR-PL decay analysis (TR-PL QY). (f) Average trap depth ΔE, exciton binding energy E_b, and average thermal escape barrier E_{th}. (g) Exciton–acoustic phonon (γ_{AC}) and exciton–LO phonon (γ_{LO}) coupling, as a function of surface passivation.

A fourth graph in Figure 3l contains the exciton enhancement functions from the different NCs, normalized for the sake of comparison to T = 500 K. It can be observed that low-temperature quenching in all NC types is dominated by the activation energy E_1 of 10–20 meV, attributed to nonradiative recombination at shallow defect states. The channel strength is increased in the OA-capped NCs film, in line with the poorer surface passivation from such capping molecules, and becomes progressively less important for DDAB, ZI, and DDAB/PbBr$_2$ ligand capping. At intermediate temperatures, thermally activated exciton dissociation becomes important; the fit-extracted parameters along with the respective functions plotted in Figure 3j indicate that the electron–hole Coulombic interaction is strongest in the ZI-capped NCs with binding energies approaching the lower bound of the 120–350 meV range reported for CsPbBr$_3$ nanoplatelets.[54,55] The exciton binding energy is slightly reduced in the NCs capped with DDAB ligands and further reduced to ~62 meV for the OA-capped NCs in agreement with the 40–60 meV range reported by the majority of the reports for such NCs.[22,32,56] Above 250 K, exciton escape via the absorption of multiple optical phonons becomes activated with the fit, yielding values of the thermal escape barrier of 250–350 meV. Exciton dissociation and exciton escape compete with the exciton detrapping process; the latter becomes activated at progressively lower temperatures as the more robust DDAB/PbBr$_2$ and ZI ligands are used, resulting in a concomitant reduction of the detrapping barrier ΔE by a factor of 2, i.e., from 49 meV in the OA-capped NCs to 24 meV for the ZI-capped particles. The reduction of the exciton detrapping energy evidences the efficient passivation of deep surface traps in the DDAB- and ZI-capped NCs, resulting in an effective recovery of the PL efficiency at ambient temperatures, as evident in the graphs of Figure 3.

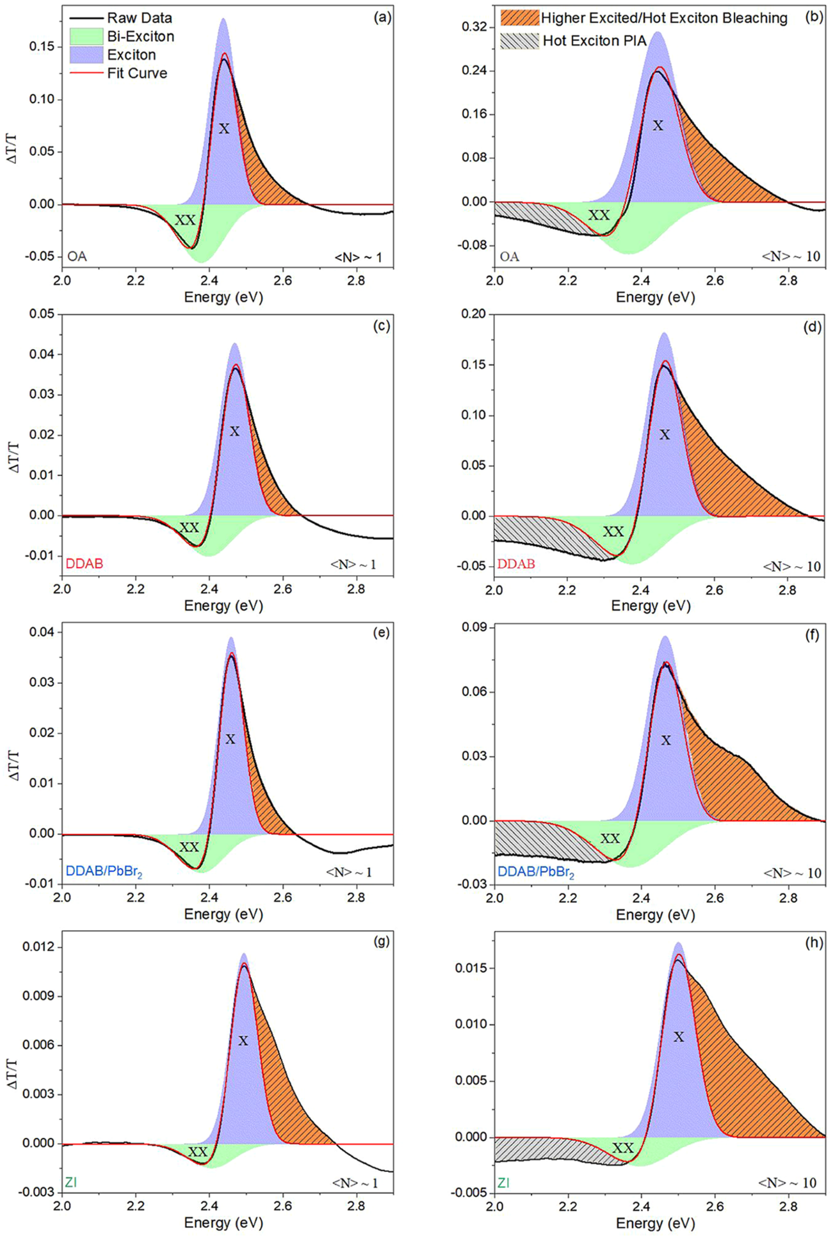

Figure 5. Transient transmission spectra at early pump-probe delay times (~1 ps) at the moderate ($\langle N \rangle \sim 1$) and high ($\langle N \rangle \sim 10$) excitation regime for (a,b) OA-, (c,d) DDAB-, (e,f) DDAB/PbBr$_2$-, and (g,h) ZI-capped CsPbBr$_3$ NC films. In the figure, the Gaussian line shape analysis, resolving the main exciton (X, purple) and biexciton (XX, green) band, is also presented. The orange-shaded area is due to the bleaching contribution of hot and higher excited exciton states. The gray PIA band evident at high photoexcitation is most probably related to absorption processes involving hot excitons.

The findings of the variable temperature PL experiments are supported by temperature-dependent transient PL (TR-PL) measurements performed across the same photoexcitation regime and within the 77−300 K temperature range. The PL decays were obtained while monitoring the PL emission peak and approximated using a biexponential model, except from the DDAB and DDAB/PbBr$_2$ ligands in which a third decay term was included to properly fit the data. The raw TR-PL data and fitted curves are displayed in Figure S3, while the extracted amplitudes and time constants for each temperature and each NC system are provided in Tables S1 and S2 for the bi- and the triple-exponential models applied to the OA-, ZI-, DDAB-, and DDAB/PbBr$_2$-capped NCs. For the former two systems, the amplitude dominant (weaker) of the two decay terms was phenomenologically assigned to the radiative lifetime τ_R (nonradiative lifetime τ_{NR}) considering the prevalence of radiative recombination in CsPbBr$_3$ NCs. Based on such an assignment and the fit extracted A_R (A_{NR}) amplitudes of the radiative (nonradiative) decay term for each NC material, the average PL lifetime τ_{av} and the radiative QY were computed using the following relations:[57]

$$\tau_{av} = \frac{A_R \tau_R^2 + A_{NR}\,\tau_{NR}^2}{A_R\,\tau_R + A_{NR}\,\tau_{NR}},\ \mathrm{QY} = \frac{A_R \tau_R}{A_R \tau_R + A_{NR} \tau_{NR}} \quad (3)$$

The calculated τ_{av} and QY values for the OA- and ZI-capped NCs are provided in Table S3, while their temperature variation is displayed in Figure 3e,h; the x-axis graph scale was chosen to match the respective scale of the SS-PL graphs displayed in the

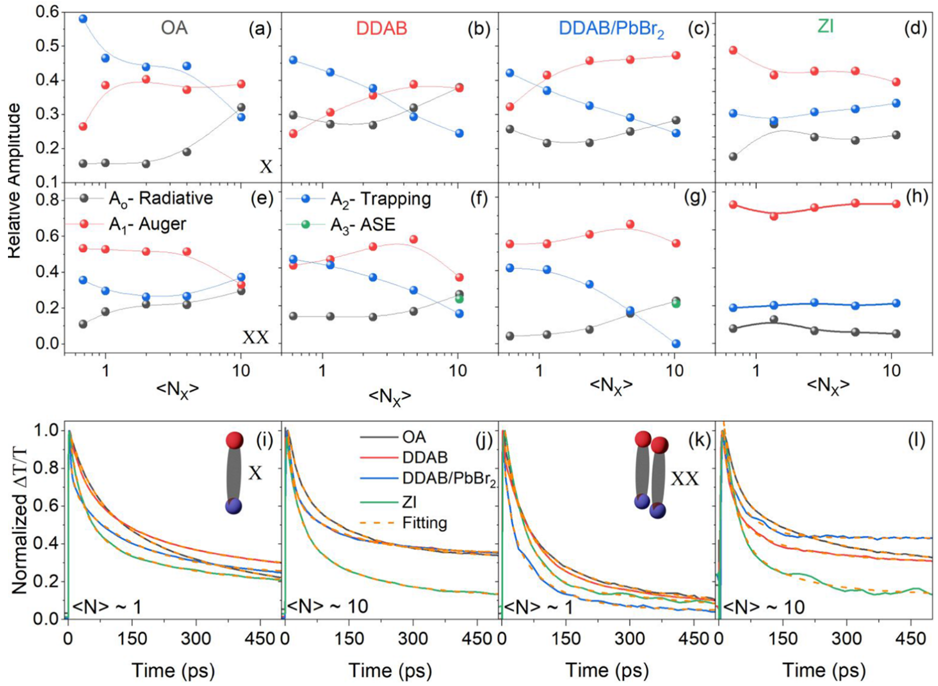

Figure 6. Transient transmission decay component amplitudes for the exciton peak of (a) OA-, (b) DDAB-, (c) DDAB/PbBr$_2$-, and (d) ZI-capped CsPbBr$_3$ NCs as a function of average number of excitons per NC. Decay component amplitudes of the biexciton band for (e) OA-, (f) DDAB-, (g) DDAB/PbBr$_2$-, and (h) ZI-capped NCs as a function of the average number of excitons per nanocrystal. Transient transmission decays for the exciton (X) band for (i) $\langle N \rangle \sim 1$ and (j) $\langle N \rangle \sim 10$ and the biexciton (XX) band for (k) $\langle N \rangle \sim 1$ and (l) $\langle N \rangle \sim 10$.

overhead (Figure 3a,d), so that a direct comparison of the data can be performed within the overlapping 77−300 K range of the two types of experiments. At room temperature, average PL lifetimes of ∼7 ns have been obtained for the OA-, DDAB-, and ZI-capped NCs and ∼12 ns for the DDAB/PbBr$_2$ NCs, in agreement with the literature reported range, i.e., ∼6−12 ns for OA NCs, 7−14 ns for DDAB-based NCs, and ∼7 ns for ZI-capped NCs.[15,35,38,40,58,59] The validity of the rather arbitrary assignment of the radiative lifetime to the dominant PL decay term and the associated estimation of the radiative yield in the two studied NC systems are confirmed by (i) the reasonably good resemblance of the temperature variation of the integrating PL and the radiative QY displayed in Figure 3 and (ii) the good matching of the QY values computed at room temperature with those estimated via integrating sphere PL experiments (blue data points and error), discussed earlier in the text. For the DDAB- and DDAB/PbBr$_2$-capped NCs, the transient PL model requires three decay components; hence, the aforementioned reasoning for the estimation of the radiative lifetime and the QY cannot be applied. Figure 3f,g instead contains the temperature variation of the average PL lifetime from such NCs that does not exhibit a direct correlation with the respective variation of the integrated PL data depicted in Figure 3b,c. The different behaviors of the NCs passivated by DDAB-based ligands are attributed to the smaller inter-NC distance in the solid state, allowed by the DDAB complex, compared to the respective NC separation defined by the oleic acid and ZI molecules. Such short interparticle distance results in superior electrical transport properties for the DDAB- compared to OA- and ZI-capped NCs, as evidenced in photoconductivity experiments presented later in the text. The shorter NC−NC distance activates stronger exciton−exciton interactions within neighboring NCs, resulting in the complex, multiexponential decays from DDAB NCs. Such an interpretation is confirmed by experiments summarized in Figure S4, which contains the results of a similar temperature-dependent PL study performed on a film spin-cast out of a DDAB/PbBr$_2$−CsPbBr$_3$ NC solution that has been diluted by 20 times compared to the nominal ∼25 g/L concentration used for all other samples in this study. The TRPL decays for such films are well described by a double, instead of a triple-exponential model, as the NC dilution weakens the NC−NC interactions.

Based on the reasoning used for the transient PL data of the OA- and ZI-capped NCs, the radiative lifetime and QY are computed for the diluted DDAB-capped NCs, with values included in Table S4. A close resemblance of the temperature dependence of the radiative yield and the integrated PL intensity can now be established, as seen Figure S4, similar to the trend observed in the data of Figure 3 for the OA- and ZI-capped NCs. This validates the phenomenological method used to estimate the radiative lifetime and radiative yield for all ligands explored, with the asterisk that it applies only to fairly diluted films of DDAB-capped NCs.

The analysis we have discussed allows us to produce the energetic models of the four studied ligands in the CsPbBr$_3$ NCs, as presented in Figure 4a−d. Each illustration contains a schematic of the NCs with their respective capping molecules and the estimated energy levels of uncorrelated electron−hole pairs, excitons, and defects. Furthermore, summary plots are included in Figure 4e−g, containing the discussed, well-defined ligand-dependent trends on the (i) PL QY; (ii) detrapping activation energy assigned to the average trap depth, ΔE; (iii) exciton binding energy E_b; (iv) average thermal escape barrier E_{th}, and (v) exciton−acoustic γ_{AC} and the exciton LO optical γ_{LO} phonon interaction couplings.

Photophysics at High Photoexcitation Densities. The impact of surface functionalization on exciton recombination in the CsPbBr$_3$ NC films was examined via transient absorption

(TA) pump probe spectroscopy, investigating the moderate to high photoexcitation regime of 0.5−10 excitons per NCs. Representative TA spectra (1 ps) after the pump pulse from probed NC systems at exciton occupation of ($\langle N\rangle \sim 1$) and ($\langle N\rangle \sim 10$) are presented in Figure 5. The data were Gaussian line fitted resolving two main TA features: (i) a broad, slowly decaying bleaching band coded X, with energies in the vicinity of the NC band-edge, assigned to the first NC excitonic transition; and (ii) a photoinduced absorption (PIA) band coded XX that evolves within a few picoseconds into a bleaching feature at ∼80 meV below the exciton. Based on the energy position, the derivative-like shape, and the amplitude sensitivity to the excitation density,[60] the XX energy band was assigned to the biexciton state.

In addition to the two main features, the high excitation spectra contain fast decaying: (i) bleaching contributions at energies above the exciton band assigned to hot and higher excited-state excitons and (ii) negative contribution at low energy most probably related to PIA processes of hot excitons.[61,62] Inspection of Figure 5 reveals that surface passivation has a minimal impact on the spectral characteristics of the X and XX bands, with small variations observed for the other transitions, i.e., a better resolved higher excitonic transition, possibly related to the $1P_h-1P_e$ exciton, in the DDAB/PbBr$_2$-capped film compared to the other three NC films. In contrast, the temporal characteristics of the X and XX states exhibit small but consistent ligand-dependent variations, as evident in the graphs of Figure 6.

The normalized decays of the exciton (X) and biexciton (XX) bands for all three studied NC systems have been fitted via the exponential decay model (4), with the third decay channel, i.e., A_3,τ_3 required only for the highest pump fluence ($<N> \sim 10$).

$$\frac{\Delta T}{T} = A_0 + A_1\,e^{-t/\tau_1} + A_2\,e^{-t/\tau_2} + A_3\,e^{-t/\tau_3} \text{ with}$$
$$A_0 + A_1 + A_2 + A_3 = 1 \quad (4)$$

The fitting extracted lifetimes appear similar in the X and XX bands for all fluences, yielding values of τ_1 in the range of 30−50 ps and τ_2 in the range of 180−220 ps. The respective relative amplitudes A_1 and A_2, as well as that of the background term A_0, though exhibit fluence-dependent trends displayed in the graphs of Figure 6a−h, which provide insight into (i) the nature of the respective three relaxation mechanisms and (ii) the impact of ligand capping on each relaxation channel. In particular, A_1 characterizing the fast decay τ_1 exhibits, apart for the ZI-capped NCs, an increasing trend with fluence for the exciton and biexciton bands; at the highest excitation density, A_1 saturates and drops, for the exciton and biexciton decay, respectively. For the case of ZI-capped NCs, the channel shows a different behavior, saturating or slightly decreasing as the exciton population is increased. Based on the excitation dependence and the observed time scales, the decay is assigned to the Auger recombination.[63] More than half of the biexcitons recombine via Auger, i.e., $A_1 > 0.5$, being the dominant quenching channel of biexcitons in all samples while significantly affecting the exciton band dynamics as well, because of the large overlap of the two bands, evidenced by the Gaussian line shape analysis of Figure 5. An interesting ligand-dependent trend can also be observed, with Auger recombination slightly but consistently being stronger in the better passivated DDAB/PbBr$_2$- and ZI-capped NCs, resulting in overall faster TA transients in such samples, as evident in Figure 6i−l. Most probably, this is a result of the improved preservation of the NC size and shape when the DDAB/PbBr$_2$ and ZI ligands are used, increasing the spectral overlap of exciton wave functions and thus the biexciton Auger recombination rate.

The second, longer ∼200 ps decay component exhibits a relative amplitude A_2 that tends to drop with fluence for excitons and biexcitons, except for the ZI-capped NCs, in which the channel strength remains unaffected by the laser excitation power. It can also be observed that the relative amplitude of the component decreases as more robust surface passivation is used, i.e., being highest for the OA-capped NCs and lower for the NCs in which a combined treatment with DDAB and PbBr$_2$ was used. Based on such anticorrelation with the NC surface quality, the channel is tentatively assigned to surface exciton/biexciton trapping. The assignment is consistent with the quenching of A_2 with fluence, as a higher exciton density results in trap saturation, suppressing the efficiency of trapping.

The background term A_0 accounts for recombination mechanisms such as radiative recombination with dynamics longer than the 500 ps probe range of our TA setup. The relative weight of the channel generally increases with fluence in both the exciton and biexciton bands, being benefited by the trap saturation and the respective quenching of the trapping term A_2. In the DDAB and DDAB/PbBr$_2$, the biexciton decays at the highest fluence of $\langle N\rangle \sim 10$ become visibly faster as an additional short decay channel A_3 with dynamics of ∼10 ps is activated, requiring the approximation of the TA transients with a triple-exponential model. Insight into the origin of this channel is provided by excitation-dependent PL experiments performed on the same films; as observed in Figure S5, the integrated PL intensity assumes a change in the slope from sublinear to superlinear above ∼35 μeV/cm^2, which roughly corresponds to $\langle N\rangle$ equal to 5 for both DDAB- and DDAB/PbBr$_2$-capped NCs. The threshold behavior is combined with emission narrowing, characteristic of the activation of the amplified spontaneous emission (ASE). The fast ∼10 ps channel observed in such NCs is then assigned to the stimulated emission, which typically originates in biexciton recombination in perovskite NCs. Interestingly, no ASE is observed in the OA- and ZI-capped NC films, consistent with the absence of the fast recombination channel in the TA transients of such samples. Based on such assignments, the suppression of the biexciton Auger amplitude A_1 observed in the DDAB- and DDAB/PbBr$_2$-capped NCs at $\langle N\rangle \sim 10$ can be interpreted as unfavorable competition with the stimulated emission process in such NCs.

Electronic communication between the CsPbBr$_3$ NCs mediated via the studied ligands was probed through photoconductivity experiments performed in lateral ITO−NC−ITO devices based on interdigitated ITO electrodes distanced by 50 μm channels. The geometry allows the probing of the hole transport within the NC channels, with the obtained photocurrent results displayed in Figure 7. The OA and ZI ligands define relatively large distances between neighboring NCs that suppress hole transport, resulting in negligible photoconductance. However, an appreciable photocurrent was recorded for devices employing NCs capped with DDAB-related ligands, with maximum current density values of ∼150 and ∼270 μA/cm^2 at 10 V, for the DDAB- and DDAB/PbBr$_2$-capped NCs, respectively. The increase in the photocurrent by a factor of almost 2 in the DDAB-capped NCs treated with PbBr$_2$ may be due to a more efficient healing of the surface traps that act as exciton/carrier quenchers.

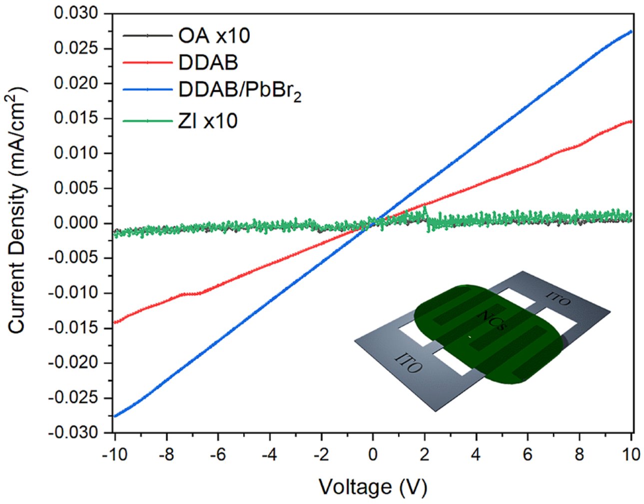

Figure 7. Ligand-dependent photocurrent density of lateral ITO-NC-ITO devices vs applied voltage. The illustration shows the device structure. Each pair of contacts is separated by 50 μm channels.

Driven by the findings of photoconductivity, perovskite light-emitting diodes (PeLEDs) based on the DDAB and DDAB/PbB$_2$ electronic-active ligands were fabricated and characterized. The electroluminescent performance of such devices is presented in Figure 8. Current density−voltage ($J-V$) characteristics are indicative of diode behavior with significantly high injected current densities, as shown in Figure 8a. In agreement with their improved photoconductive performance, PeLEDs based on DDAB/PbBr$_2$-capped NCs exhibit better electrical injection properties at a higher bias voltage in comparison with DDAB-treated NC PeLEDs. As seen in Figure 8b, DDAB/PbBr$_2$-based devices have a lower turn on voltage (voltage at which luminance reach the value of 10 cd/m^2) of ∼3.0 V compared to the ∼3.5 V of DDAB-based PeLEDs, in line with the better charge injection properties of the former NCs. Despite that, both devices exhibit high luminance values, with DDAB-based LEDs showing the maximum luminance of 3135 cd/m^2 overcoming the respective 2265 cd/m^2 value of the DDAB/PbBr$_2$-based devices. To investigate the efficiency of the fabricated devices, current efficiency with respect to current density was plotted, as presented in Figure 8d and power efficacy−luminance in Figure 8c. Both current efficiency and power efficacy are significantly higher in the device using DDAB/PbBr$_2$-capped NCs (1.9 cd/A, 1.7 lm/W, respectively) in comparison with the DDAB-decorated material (0.4 cd/A, 0.3 lm/W, respectively). This can be rationalized by some of the discussed findings that indicate improvements in the structural integrity and optoelectronic properties of the former compared

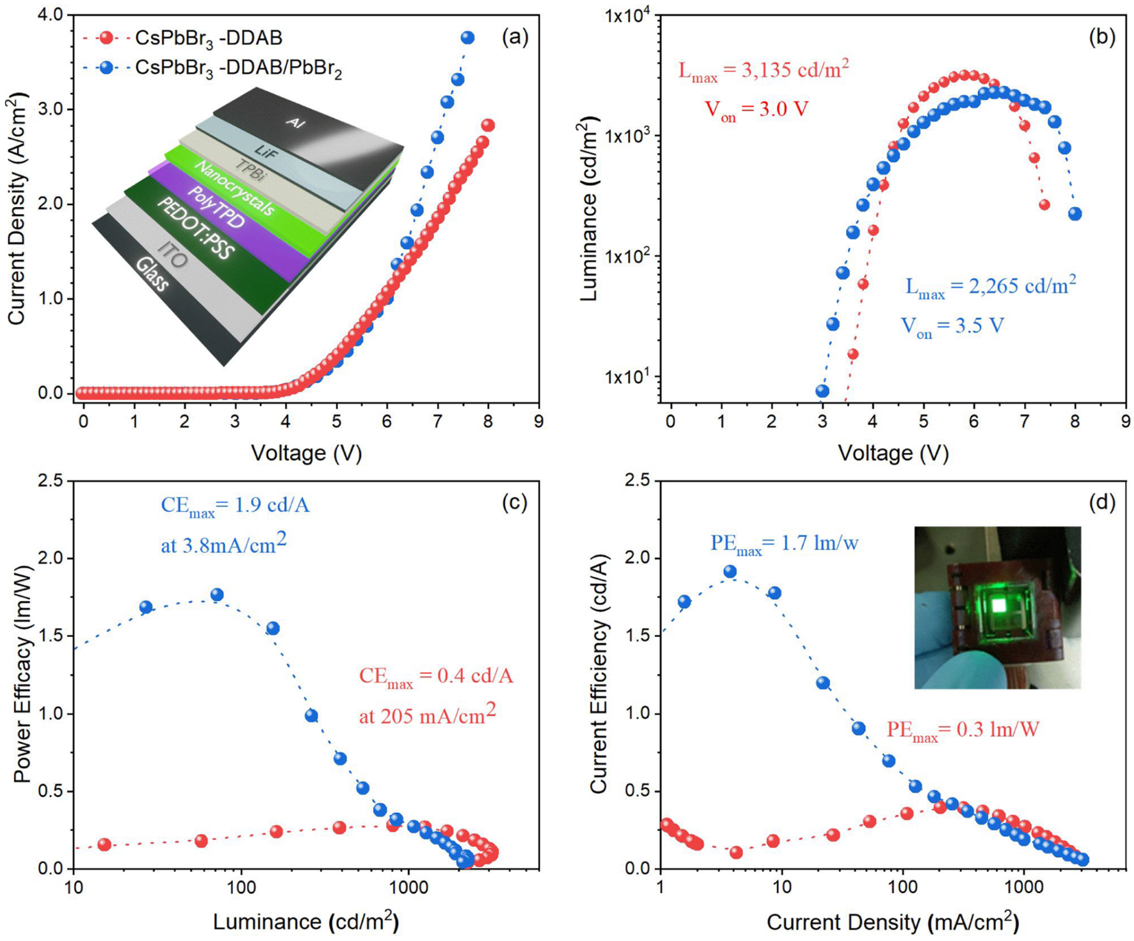

Figure 8. Electroluminescent performance of PeLEDs using DDAB- and DDAB/PbBr2-treated NCs summarized into (a) current density—voltage ($J-V$) graph (the inset shows an illustration of the device structure), (b) luminance−voltage behavior (LV), (c) current efficiency−current density graph, and (d) power efficacy−luminance characteristic plot (the inset shows the photograph of an operating 9 mm^2 perovskite LED device, based on the DDAB/PbBr$_2$ ligand treatment).

to the latter NCs. Such metrics include the observation of small but reproducible increases in the PL QY (by ~5%) and the exciton binding energy (by ~5 meV) and a lowering of the average trap depth (by ~6 meV) combined with the improved turn-on LED voltage (by 0.5 V), when a combined treatment with DDAB and $PbBr_2$ is used. As a final comment, it can be observed that in the high current density range, the efficiency of both types of PeLEDs deteriorates fast, most probably because of the structural and thermal degradation of the NCs.

As a final characterization step, the ability of each ligand shell to protect the NC surface against moisture was investigated, by immersing the NC films into water while monitoring their PL in real time. The raw PL data and PL emission efficiency versus water soaking time is displayed in Figure S6. OA- and ZI-capped NC films are the least water-tolerant, showing a fast emission quenching in the range of a few seconds, with the main difference being that the latter films better preserve the emission line shape within their short, underwater lifetime. In contrast, DDAB-based ligands better protect the NC core against water, allowing the NCs to maintain their PL line shape and intensity for several minutes.

■ CONCLUSIONS

In summary, a systematic spectroscopic and device characterization study was performed to understand the impact of four surface passivation routes based on OA, ZI 3-(*N*,*N*-dimethyloctadecylammonio)propansulfonate, DDAB, and DDAB–$PbBr_2$ treatments on the solid-state optoelectronic properties of weakly confined $CsPbBr_3$ NCs. The ligand-dependent trends of NC exciton parameters such as binding energy, phonon coupling, trapping depth, Auger recombination, and radiative lifetime/yield have been established, while the impact of surface passivation on figures of merit interesting for applications such as the ASE threshold, the photoconductive and electroluminescent performance, and the NC stability in a harsh water environment has been explored. Overall, $CsPbBr_3$ NCs subjected to the DDAB–$PbBr_2$ treatment appear highly promising for photoluminescence, electroluminescence, and lasing applications. ZI-capped NCs exhibit an even higher luminescence efficiency and stronger exciton binding in the solid state; however, this comes at the expense of their transport properties inhibited by the long-chain ligand shell and their moisture sensitivity; further optimization or encapsulation in host matrixes may render such NCs also highly promising for applications such as remote light emitters and downconverters.

■ ASSOCIATED CONTENT

Supporting Information

The Supporting Information is available free of charge at https://pubs.acs.org/doi/10.1021/acsanm.1c00558.

> Size distribution derived from TEM analysis; optical properties of the NC colloids; PL decays and multi-exponential fits from spin-cast NC films; tables with PL lifetime constants and amplitudes from NC films; optical properties of DDAB/$PbBr_2$–$CsPbBr_3$ NC films produced out of a diluted (20 times) NC solution; ASE studies of NC films; NC emission stability under water soaking (PDF)

■ AUTHOR INFORMATION

Corresponding Author

Grigorios Itskos – *Department of Physics, Experimental Condensed Matter Physics Laboratory, University of Cyprus, Nicosia 1678, Cyprus*; orcid.org/0000-0003-3971-3801; Email: itskos@ucy.ac.cy

Authors

Andreas Manoli – *Department of Physics, Experimental Condensed Matter Physics Laboratory, University of Cyprus, Nicosia 1678, Cyprus*

Paris Papagiorgis – *Department of Physics, Experimental Condensed Matter Physics Laboratory, University of Cyprus, Nicosia 1678, Cyprus*; orcid.org/0000-0002-6627-0463

Marios Sergides – *Department of Physics, Laboratory of Ultrafast Science, University of Cyprus, Nicosia 1678, Cyprus*

Caterina Bernasconi – *Institute of Inorganic Chemistry, Department of Chemistry and Applied Biosciences, ETH Zürich, Zürich CH-8093, Switzerland; Laboratory for Thin Films and Photovoltaics, Empa – Swiss Federal Laboratories for Materials Science and Technology, Dübendorf CH-8600, Switzerland*

Modestos Athanasiou – *Department of Physics, Experimental Condensed Matter Physics Laboratory, University of Cyprus, Nicosia 1678, Cyprus*; orcid.org/0000-0003-1684-9482

Sergey Pozov – *Molecular Electronics and Photonics Research Unit, Department of Mechanical Engineering and Materials Science and Engineering, Cyprus University of Technology, Limassol 3603, Cyprus*

Stelios A. Choulis – *Molecular Electronics and Photonics Research Unit, Department of Mechanical Engineering and Materials Science and Engineering, Cyprus University of Technology, Limassol 3603, Cyprus*; orcid.org/0000-0002-7899-6296

Maryna I. Bodnarchuk – *Laboratory for Thin Films and Photovoltaics, Empa – Swiss Federal Laboratories for Materials Science and Technology, Dübendorf CH-8600, Switzerland*; orcid.org/0000-0001-6597-3266

Maksym V. Kovalenko – *Institute of Inorganic Chemistry, Department of Chemistry and Applied Biosciences, ETH Zürich, Zürich CH-8093, Switzerland; Laboratory for Thin Films and Photovoltaics, Empa – Swiss Federal Laboratories for Materials Science and Technology, Dübendorf CH-8600, Switzerland*; orcid.org/0000-0002-6396-8938

Andreas Othonos – *Department of Physics, Laboratory of Ultrafast Science, University of Cyprus, Nicosia 1678, Cyprus*

Complete contact information is available at: https://pubs.acs.org/10.1021/acsanm.1c00558

Notes

The authors declare no competing financial interest.

■ ACKNOWLEDGMENTS

This work was financially supported by the Research and Innovation Foundation of Cyprus under the “New Strategic Infrastructure Units-Young Scientists” Program (Grant Agreement no. “INFRASTRUCTURES/1216/0004,” Acronym “NANOSONICS”).

■ REFERENCES

(1) Kovalenko, M. V.; Protesescu, L.; Bodnarchuk, M. I. Properties and Potential Optoelectronic Applications of Lead Halide Perovskite Nanocrystals. *Science* **2017**, *358*, 745–750.

(2) Protesescu, L.; Yakunin, S.; Bodnarchuk, M. I.; Krieg, F.; Caputo, R.; Hendon, C. H.; Xi Yang, R.; Walsh, A.; Kovalenko, M. V. Nanocrystals of Cesium Lead Halide Perovskites ($CsPbX_3$, X = Cl, Br, and I): Novel Optoelectronic Materials Showing Bright Emission with Wide Color Gamut. *Nano Lett.* **2015**, *15*, 3692−3696.

(3) Huang, H.; Polavarapu, L.; Sichert, J. A.; Susha, A. S.; Urban, A. S.; Rogach, A. L. Colloidal Lead Halide Perovskite Nanocrystals: Synthesis, Optical Properties and Applications. *NPG Asia Mater.* **2016**, *8*, e328−e328.

(4) Shamsi, J.; Urban, A. S.; Imran, M.; De Trizio, L.; Manna, L. Metal Halide Perovskite Nanocrystals: Synthesis, Post-Synthesis Modifications, and Their Optical Properties. *Chem. Rev.* **2019**, *119*, 3296−3348.

(5) Akkerman, Q. A.; Rainò, G.; Kovalenko, M. V.; Manna, L. Genesis, Challenges and Opportunities for Colloidal Lead Halide Perovskite Nanocrystals. *Nat. Mater.* **2018**, *17*, 394−405.

(6) Krieg, F.; Ochsenbein, S. T.; Yakunin, S.; Ten Brinck, S.; Aellen, P.; Süess, A.; Clerc, B.; Guggisberg, D.; Nazarenko, O.; Shynkarenko, Y.; Kumar, S.; Shih, C.-J.; Infante, I.; Kovalenko, V. M. Colloidal CsPbX3 (X = Cl, Br, I) Nanocrystals 2.0: Zwitterionic Capping Ligands for Improved Durability and Stability. *ACS Energy Lett.* **2018**, *3*, 641−646.

(7) Wang, C.; Chesman, A. S. R.; Jasieniak, J. J. Stabilizing the Cubic Perovskite Phase of $CsPbI_3$ Nanocrystals by Using an Alkyl Phosphinic Acid. *Chem. Commun.* **2017**, *53*, 232−235.

(8) Liu, F.; Zhang, Y.; Ding, C.; Kobayashi, S.; Izuishi, T.; Nakazawa, N.; Toyoda, T.; Ohta, T.; Hayase, S.; Minemoto, T.; Yoshino, K.; Dai, S.; Shen, Q. Highly Luminescent Phase-Stable $CsPbI_3$ Perovskite Quantum Dots Achieving Near 100% Absolute Photoluminescence Quantum Yield. *ACS Nano* **2017**, *11*, 10373−10383.

(9) Liu, M.; Li, Z.; Zheng, W.; Kong, L.; Li, L. Improving the Stability of $CsPbBr_3$ Perovskite Nanocrystals by Peroxides Post-Treatment. *Front. Mater.* **2019**, *6*, 1−8.

(10) Bodnarchuk, M. I.; Boehme, S. C.; Ten Brinck, S.; Bernasconi, C.; Shynkarenko, Y.; Krieg, F.; Widmer, R.; Aeschlimann, B.; Günther, D.; Kovalenko, M. V.; Infant, I. Rationalizing and Controlling the Surface Structure and Electronic Passivation of Cesium Lead Halide Nanocrystals. *ACS Energy Lett.* **2019**, *4*, 63−74.

(11) Zheng, C.; Bi, C.; Huang, F.; Binks, D.; Tian, J. Stable and Strong Emission $CsPbBr_3$ Quantum Dots by Surface Engineering for High-Performance Optoelectronic Films. *ACS Appl. Mater. Interfaces* **2019**, *11*, 25410−25416.

(12) Lignos, I.; Stavrakis, S.; Nedelcu, G.; Protesescu, L.; Demello, A. J.; Kovalenko, M. V. Synthesis of Cesium Lead Halide Perovskite Nanocrystals in a Droplet-Based Microfluidic Platform: Fast Parametric Space Mapping. *Nano Lett.* **2016**, *16*, 1869−1877.

(13) Woo, J. Y.; Kim, Y.; Bae, J.; Kim, T. G.; Kim, J. W.; Lee, D. C.; Jeong, S. Highly Stable Cesium Lead Halide Perovskite Nanocrystals through in Situ Lead Halide Inorganic Passivation. *Chem. Mater.* **2017**, *29*, 7088−7092.

(14) Pan, J.; Shang, Y.; Yin, J.; De Bastiani, M.; Peng, W.; Dursun, I.; Sinatra, L.; El-Zohry, A. M.; Hedhili, M. N.; Emwas, A.-H.; Mohammed, F. O.; Ning, Z.; Bakr, M. O. Bidentate Ligand-Passivated CsPbI3 Perovskite Nanocrystals for Stable Near-Unity Photoluminescence Quantum Yield and Efficient Red Light-Emitting Diodes. *J. Am. Chem. Soc.* **2018**, *140*, 562−565.

(15) Di Stasio, F.; Christodoulou, S.; Huo, N.; Konstantatos, G. Near-Unity Photoluminescence Quantum Yield in CsPbBr3 Nanocrystal Solid-State Films via Postsynthesis Treatment with Lead Bromide. *Chem. Mater.* **2017**, *29*, 7663−7667.

(16) Bohn, B. J.; Tong, Y.; Gramlich, M.; Lai, M. L.; Döblinger, M.; Wang, K.; Hoye, R. L. Z.; Müller-Buschbaum, P.; Stranks, S. D.; Urban, A. S.; Polavarapu, L.; Feldmann, J. Boosting Tunable Blue Luminescence of Halide Perovskite Nanoplatelets through Postsynthetic Surface Trap Repair. *Nano Lett.* **2018**, *18*, 5231−5238.

(17) Koscher, B. A.; Swabeck, J. K.; Bronstein, N. D.; Alivisatos, A. P. Essentially Trap-Free $CsPbBr_3$ Colloidal Nanocrystals by Postsynthetic Thiocyanate Surface Treatment. *J. Am. Chem. Soc.* **2017**, *139*, 6566−6569.

(18) Pan, J.; Sarmah, S. P.; Murali, B.; Dursun, I.; Peng, W.; Parida, M. R.; Liu, J.; Sinatra, L.; Alyami, N.; Zhao, C.; Alarousu, E.; Ng, K. T.; Ooi, S. B.; Bakr, M. O.; Mohammed, F. O. Air-Stable Surface-Passivated Perovskite Quantum Dots for Ultra-Robust, Single- and Two-Photon-Induced Amplified Spontaneous Emission. *J. Phys. Chem. Lett.* **2015**, *6*, 5027−5033.

(19) Huang, S.; Wang, B.; Zhang, Q.; Li, Z.; Shan, A.; Li, L. Postsynthesis Potassium-Modification Method to Improve Stability of $CsPbBr_3$ Perovskite Nanocrystals. *Adv. Opt. Mater.* **2018**, *6*, No. 1701106.

(20) Wu, Y.; Wei, C.; Li, X.; Li, Y.; Qiu, S.; Shen, W.; Cai, B.; Sun, Z.; Yang, D.; Deng, Z.; Zeng, H. In Situ Passivation of $PbBr_6^{4-}$ Octahedra toward Blue Luminescent CsPbBr3 Nanoplatelets with Near 100% Absolute Quantum Yield. *ACS Energy Lett.* **2018**, *3*, 2030−2037.

(21) Zhou, Q.; Bai, Z.; Lu, W. G.; Wang, Y.; Zou, B.; Zhong, H. In Situ Fabrication of Halide Perovskite Nanocrystal-Embedded Polymer Composite Films with Enhanced Photoluminescence for Display Backlights. *Adv. Mater.* **2016**, *28*, 9163−9168.

(22) Guhrenz, C.; Benad, A.; Ziegler, C.; Haubold, D.; Gaponik, N.; Eychmüller, A. Solid-State Anion Exchange Reactions for Color Tuning of CsPbX3 Perovskite Nanocrystals. *Chem. Mater.* **2016**, *28*, 9033−9040.

(23) Huang, H.; Chen, B.; Wang, Z.; Hung, T. F.; Susha, A. S.; Zhong, H.; Rogach, A. L. Water Resistant $CsPbX_3$ Nanocrystals Coated with Polyhedral Oligomeric Silsesquioxane and Their Use as Solid State Luminophores in All-Perovskite White Light-Emitting Devices. *Chem. Sci.* **2016**, *7*, 5699−5703.

(24) Meyns, M.; Perálvarez, M.; Heuer-Jungemann, A.; Hertog, W.; Ibáñez, M.; Nafria, R.; Genç, A.; Arbiol, J.; Kovalenko, M. V.; Carreras, J.; Cabot, A.; Kanaras, G. A. Polymer-Enhanced Stability of Inorganic Perovskite Nanocrystals and Their Application in Color Conversion LEDs. *ACS Appl. Mater. Interfaces* **2016**, *8*, 19579−19586.

(25) Quan, L. N.; Quintero-Bermudez, R.; Voznyy, O.; Walters, G.; Jain, A.; Fan, J. Z.; Zheng, X.; Yang, Z.; Sargent, E. H. Highly Emissive Green Perovskite Nanocrystals in a Solid State Crystalline Matrix. *Adv. Mater.* **2017**, *29*, No. 1605945.

(26) Raja, S. N.; Bekenstein, Y.; Koc, M. A.; Fischer, S.; Zhang, D.; Lin, L.; Ritchie, R. O.; Yang, P.; Alivisatos, A. P. Encapsulation of Perovskite Nanocrystals into Macroscale Polymer Matrices: Enhanced Stability and Polarization. *ACS Appl. Mater. Interfaces* **2016**, *8*, 35523−35533.

(27) Xu, L.; Chen, J.; Song, J.; Li, J.; Xue, J.; Dong, Y.; Cai, B.; Shan, Q.; Han, B.; Zeng, H. Double-Protected All-Inorganic Perovskite Nanocrystals by Crystalline Matrix and Silica for Triple-Modal Anti-Counterfeiting Codes. *ACS Appl. Mater. Interfaces* **2017**, *9*, 26556−26564.

(28) González-Pedro, V.; Veldhuis, S. A.; Begum, R.; Bañuls, M. J.; Bruno, A.; Mathews, N.; Mhaisalkar, S.; Maquieira, Á. Recovery of Shallow Charge-Trapping Defects in CsPbX3 Nanocrystals through Specific Binding and Encapsulation with Amino-Functionalized Silanes. *ACS Energy Lett.* **2018**, *3*, 1409−1414.

(29) Zhang, X.; Wang, H. C.; Tang, A. C.; Lin, S. Y.; Tong, H. C.; Chen, C. Y.; Lee, Y. C.; Tsai, T. L.; Liu, R. S. Robust and Stable Narrow-Band Green Emitter: An Option for Advanced Wide-Color-Gamut Backlight Display. *Chem. Mater.* **2016**, *28*, 8493−8497.

(30) Yang, D.; Li, X.; Zeng, H. Surface Chemistry of All Inorganic Halide Perovskite Nanocrystals: Passivation Mechanism and Stability. *Adv. Mater. Interfaces* **2018**, *5*, 1−13.

(31) Papagiorgis, P.; Protesescu, L.; Kovalenko, M.; Othonos, A.; Itskos, G. Long-Lived Hot Carriers in Formamidinium Lead Iodide Nanocrystals. *J. Phys. Chem. C* **2017**, *121*, 12434−12440.

(32) Heidrich, K.; Schäfer, W.; Schreiber, M.; Söchtig, J.; Trendel, G.; Treusch, J.; Grandke, T.; Stolz, H. J. Electronic Structure, Photoemission Spectra, and Vacuum-Ultraviolet Optical Spectra of $CsPbCl_3$ and $CsPbBr_3$. *Phys. Rev. B* **1981**, *24*, No. 5642.

(33) Ramade, J.; Andriambariarijaona, L. M.; Steinmetz, V.; Goubet, N.; Legrand, L.; Barisien, T.; Bernardot, F.; Testelin, C.; Lhuillier, E.; Bramati, A.; Chamarro, M. Fine Structure of Excitons and Electron-Hole Exchange Energy in Polymorphic $CsPbBr_3$ Single Nanocrystals. *Nanoscale* **2018**, *10*, 6393−6401.

(34) Rudin, S.; Reinecke, T. L.; Segall, B. Temperature-Dependent Exciton Linewidths in Semiconductors. *Phys. Rev. B* **1990**, *42*, 11218−11231.

(35) Pan, J.; Quan, L. N.; Zhao, Y.; Peng, W.; Murali, B.; Sarmah, S. P.; Yuan, M.; Sinatra, L.; Alyami, N. M.; Liu, J.; Yassitepe, E.; Yang, Z.; Voznyy, O.; Comin, R.; Hedhili, N. M.; Mohammed, F. O.; Lu, H. Z.; Kim, H. D.; Sargent, H. E.; Bakr, M. O. See fewer authors Highly Efficient Perovskite-Quantum-Dot Light-Emitting Diodes by Surface Engineering. *Adv. Mater.* **2016**, *28*, 8718−8725.

(36) Chen, Y.; Smock, S. R.; Flintgruber, A. H.; Perras, F. A.; Brutchey, R. L.; Rossini, A. J. Surface Termination of $CsPbBr_3$ Perovskite Quantum Dots Determined by Solid-State NMR Spectroscopy. *J. Am. Chem. Soc.* **2020**, *142*, 6117−6127.

(37) Zhu, B.-S.; Li, H.-Z.; Ge, J.; Li, H.-D.; Yin, Y.-C.; Wang, K.-H.; Chen, C.; Yao, J.-S.; Zhang, Q.; Yao, H.-B. Room Temperature Precipitated Dual Phase $CsPbBr_3$-$CsPb_2Br_5$ Nanocrystals for Stable Perovskite Light Emitting Diodes. *Nanoscale* **2018**, *10*, 19262−19271.

(38) Papagiorgis, P. G.; Manoli, A.; Alexiou, A.; Karacosta, P.; Karagiorgis, X.; Papaparaskeva, G.; Bodnarchuk, M.; Kovalenko, M. V.; Krasia, T.; Itskos, G. Robust Hydrophobic and Hydrophilic Polymer Fibers Sensitized by Inorganic and Hybrid Lead Halide Perovskite Nanocrystal Emitters. *Front. Chem.* **2019**, *7*, 87.

(39) Ji Ruan, L.; Tang, B.; Ma, Y. Improving the Stability of CsPbBr3 Nanocrystals in Ethanol by Capping with PbBr2-Adlayers. *J. Phys. Chem. C* **2019**, *123*, 11959−11967.

(40) Krieg, F.; Sercel, P. C.; Burian, M.; Andrusiv, H.; Bodnarchuk, M. I.; Stöferle, T.; Mahrt, R. F.; Naumenko, D.; Amenitsch, H.; Rainò, G.; Kovalenko, V. M. Monodisperse Long-Chain Sulfobetaine-Capped $CsPbBr_3$ Nanocrystals and Their Superfluorescent Assemblies. *ACS Cent. Sci.* **2021**, *7*, 135−144.

(41) Savenije, T. J.; Ponseca, C. S.; Kunneman, L.; Abdellah, M.; Zheng, K.; Tian, Y.; Zhu, Q.; Canton, S. E.; Scheblykin, I. G.; Pullerits, T.; Yartsev, A.; Sundström, V. Thermally Activated Exciton Dissociation and Recombination Control the Carrier Dynamics in Organometal Halide Perovskite. *J. Phys. Chem. Lett.* **2014**, *5*, 2189−2194.

(42) Milot, R. L.; Eperon, G. E.; Snaith, H. J.; Johnston, M. B.; Herz, L. M. Temperature-Dependent Charge-Carrier Dynamics in $CH_3NH_3PbI_3$ Perovskite Thin Films. *Adv. Funct. Mater.* **2015**, *25*, 6218−6227.

(43) Oga, H.; Saeki, A.; Ogomi, Y.; Hayase, S.; Seki, S. Improved Understanding of the Electronic and Energetic Landscapes of Perovskite Solar Cells: High Local Charge Carrier Mobility, Reduced Recombination, and Extremely Shallow Traps. *J. Am. Chem. Soc.* **2014**, *136*, 13818−13825.

(44) Iaru, C. M.; Geuchies, J. J.; Koenraad, P. M.; Vanmaekelbergh, D.; Silov, A. Y. Strong Carrier−Phonon Coupling in Lead Halide Perovskite Nanocrystals. *ACS Nano* **2017**, *11*, 11024−11030.

(45) Ijaz, P.; Imran, M.; Márcio, M.; Soares, M.; Tolentino, H. C. N.; Martín-García, B.; Giannini, C.; Moreels, I.; Manna, L.; Krahne, R. Composition-, Size-, and Surface Functionalization-Dependent Optical Properties of Lead Bromide Perovskite Nanocrystals. *J. Phys. Chem. Lett.* **2020**, *11*, 2079−2085.

(46) Han, Q.; Wu, W.; Liu, W.; Yang, Q.; Yang, Y. Temperature-Dependent Photoluminescence of $CsPbX_3$ Nanocrystal Films. *J. Lumin.* **2018**, *198*, 350−356.

(47) Saran, R.; Heuer-Jungemann, A.; Kanaras, A. G.; Curry, R. J. Giant Bandgap Renormalization and Exciton-Phonon Scattering in Perovskite Nanocrystals. *Adv. Opt. Mater.* **2017**, *5*, No. 1700231.

(48) Diroll, B. T.; Zhou, H.; Schaller, R. D. Low-Temperature Absorption, Photoluminescence, and Lifetime of $CsPbX_3$ (X = Cl, Br, I) Nanocrystals. *Adv. Funct. Mater.* **2018**, *28*, 1−7.

(49) Stoumpos, C. C.; Malliakas, C. D.; Peters, J. A.; Liu, Z.; Sebastian, M.; Im, J.; Chasapis, T. C.; Wibowo, A. C.; Chung, D. Y.; Freeman, A. J.; Wessels, W.; Kanatzidis, G. M. Crystal Growth of the Perovskite Semiconductor $CsPbBr_3$: A New Material for High-Energy Radiation Detection. *Cryst. Growth Des.* **2013**, *13*, 2722−2727.

(50) Ganguly, A. K.; Birman, J. L. Theory of Lattice Raman Scattering in Insulators. *Phys. Rev.* **1967**, *162*, 806−816.

(51) Motti, S. G.; Krieg, F.; Ramadan, A. J.; Patel, J. B.; Snaith, H. J.; Kovalenko, M. V.; Johnston, M. B.; Herz, L. M. $CsPbBr_3$ Nanocrystal Films: Deviations from Bulk Vibrational and Optoelectronic Properties. *Adv. Funct. Mater.* **2020**, *30*, No. 1909904.

(52) Woo, H. C.; Choi, J. W.; Shin, J.; Chin, S.-H.; Ann, M. H.; Lee, C.-L. Temperature-Dependent Photoluminescence of $CH_3NH_3PbBr_3$ Perovskite Quantum Dots and Bulk Counterparts. *J. Phys. Chem. Lett.* **2018**, *9*, 4066−4074.

(53) Morello, G.; De Giorgi, M.; Kudera, S.; Manna, L.; Cingolani, R.; Anni, M. Temperature and Size Dependence of Nonradiative Relaxation and Exciton-Phonon Coupling in Colloidal CdTe Quantum Dots. *J. Phys. Chem. C* **2007**, *111*, 5846−5849.

(54) Li, Q.; Lian, T. Ultrafast Charge Separation in Two-Dimensional CsPbBr 3 Perovskite Nanoplatelets. *J. Phys. Chem. Lett.* **2019**, *10*, 566−573.

(55) Vale, B. R. C.; Socie, E.; Burgos-Caminal, A.; Bettini, J.; Schiavon, M. A.; Moser, J. E. Exciton, Biexciton, and Hot Exciton Dynamics in $CsPbBr_3$ Colloidal Nanoplatelets. *J. Phys. Chem. Lett.* **2020**, *11*, 387−394.

(56) Shinde, A.; Gahlaut, R.; Mahamuni, S. Low-Temperature Photoluminescence Studies of CsPbBr3 Quantum Dots. *J. Phys. Chem. C* **2017**, *121*, 14872−14878.

(57) Lakowicz, J. R. *Principles of Fluorescence Spectroscopy*; Springer: Boston, MA, 2006.

(58) Ahmed, T.; Seth, S.; Samanta, A. Boosting the Photoluminescence of $CsPbX_3$ (X = Cl, Br, I) Perovskite Nanocrystals Covering a Wide Wavelength Range by Postsynthetic Treatment with Tetrafluoroborate Salts. *Chem. Mater.* **2018**, *30*, 3633−3637.

(59) Dubose, J. T.; Kamat, P. V. Surface Chemistry Matters. How Ligands Influence Excited State Interactions between $CsPbBr_3$ and Methyl Viologen. *J. Phys. Chem. C* **2020**, *124*, 12990−12998.

(60) Makarov, N. S.; Guo, S.; Isaienko, O.; Liu, W.; Robel, I.; Klimov, V. I. Spectral and Dynamical Properties of Single Excitons, Biexcitons, and Trions in Cesium-Lead-Halide Perovskite Quantum Dots. *Nano Lett.* **2016**, *16*, 2349−2362.

(61) Li, Y.; Lai, R.; Luo, X.; Liu, X.; Ding, T.; Lu, X.; Wu, K. On the Absence of a Phonon Bottleneck in Strongly Confined $CsPbBr_3$ Perovskite Nanocrystals. *Chem. Sci.* **2019**, *10*, 5983−5989.

(62) Mondal, N.; De, A.; Das, S.; Paul, S.; Samanta, A. Ultrafast Carrier Dynamics of Metal Halide Perovskite Nanocrystals and Perovskite-Composites. *Nanoscale* **2019**, *11*, 9796−9818.

(63) Li, Y.; Ding, T.; Luo, X.; Chen, Z.; Liu, X.; Lu, X.; Wu, K. Biexciton Auger Recombination in Mono-Dispersed, Quantum-Confined $CsPbBr_3$ Perovskite Nanocrystals Obeys Universal Volume-Scaling. *Nano Res.* **2019**, *12*, 619−623.